Demonstration of moleculelike normal modes of Coulombic three-body systems in hyperspherical coordinates

Xian-Hui Liu,* Z. Chen, and C. D. Lin
Department of Physics, Kansas State University, Manhattan, Kansas 66506-2601
(Received 13 May 1991)

The adiabatic channel wave functions of Coulombic three-body systems are investigated in mass-weighted hyperspherical coordinates. We consider the ABA Coulombic systems, where two of the particles are identical, and examine the density distribution functions at fixed hyperradii R for different systems as the mass ratio $\lambda = m_A/m_B$ varies from the atomic limit ($\lambda \to 0$, as in H^-) to the molecular limit ($\lambda \to \infty$, as in H_2^+). The bonding and antibonding as well as the rovibrational characters of the three-body systems are illustrated by these density plots.

PACS number(s): 31.20.Tz; 31.10.+z; 31.15.+q

I. INTRODUCTION

The discovery of moleculelike normal modes [1–3] of a pair of electrons in doubly excited states of atoms has furnished a new perspective on the study of electron correlations [4]. The two electrons perform motion akin to the rotational and vibrational motion of a floppy ABA molecule, where A represents the electron and B the nucleus. The rovibrator model was first discovered from the energy-level structure of doubly excited states within the group-theoretical framework [5]. A more direct visualization was achieved by the partial display of the wave functions in the conventional independent-particle coordinates [6] and in hyperspherical coordinates [2–7].

The original group-theoretical approach [8] derived two new quantum numbers, K and T, which replace the ℓ_1 and ℓ_2 quantum numbers of the two electrons used in the independent-particle model. Later works showed that the K and T quantum numbers can be interpreted as similar to the bending vibrational quantum number $v_2 = N - K - 1$ and the vibrational angular momentum $\ell_v = T$ of a linear ABA molecule [6–9]. A further analogy was taken by treating the H^- ion similar to the molecular H_2^+ ion [10]. In the latter approach the interelectronic distance r_{12} is treated as the adiabatic parameter, similar to the role of the internuclear distance in the Born-Oppenheimer approximation for the molecule, and the quantum numbers K and T can also be identified with the H_2^+ molecular quantum numbers n_ξ and m where n_ξ is the quantum number in the spheroidal parabolic coordinate ξ and m is the projection of the orbital quantum number along the internuclear axis. A summary of these relations was given in Ref. [10(b)] as well as in Appendix A of Ref. [11].

The equivalence of these different sets of approximate quantum numbers implies that there are general characteristics in Coulombic three-body systems, ABA, where the physical properties do not depend sensitively on the masses of the particles in the system. Defining $\lambda = m_A/m_B$, we note that the K and T quantum numbers were used for $\lambda \ll 1$, v_2 and ℓ_v were used for $\lambda \cong 1$, and n_ξ and m were used for $\lambda \gg 1$. The equivalence of these systems motivated us to find a unifying theoretical framework to treat Coulombic three-body systems of arbitrary masses.

In two previous papers [11, 12] we showed that the mass-weighted hyperspherical coordinates provide a convenient basis for studying general three-body systems. By treating the hyperradius as the adiabatic parameter, a computational procedure was developed by Chen and Lin [11] where the adiabatic potential curves for arbitrary mass ratio λ were calculated. The equivalence among the above three sets of descriptions becomes evident by comparing the adiabatic potential curves for different λ's. In particular, the rovibrational behavior of the ABA system has been identified for a certain class of states where its existence does not require that the mass of particle A be large compared to the mass of particle B, as commonly assumed in the case of H_2^+. Rather, the rovibrational behavior was attributed to those states that are localized near the saddle point of the potential surface. It is the small vibrations near the saddle point that produce the rovibrational spectra. In fact, without imposing any constraints on the masses of particle A and particle B, the molecular rovibrator structure emerges from the calculated adiabatic potential curves for a certain class of states for systems like $e^-e^+e^-$ and H^-. Thus the traditional condition of large masses of the constituent particles for the existence of rovibrational spectra is too restrictive.

The results of Ref. [11] also indicate that, while to first order there is a complete equivalence among the approximate quantum numbers from different regions of λ's, deviations from the rovibrational behaviors do become more significant as the value of λ decreases and for states that are not localized near the saddle point. For the latter states the deviation is so large in the small-λ limit that the rovibrational behavior is lost. For these states, particle B tends to stay closer to one of the two identical particles A such that a description closer to the independent-particle model becomes more relevant. Such states can be partially inferred from the variation of the

calculated potential curves with λ, but more definite illustrations can be achieved only by analyzing the wave functions or the density distributions.

In this paper we compare the density distributions for different states of Coulombic three-body systems at fixed-scaled hyperradii in the body frame to illustrate the shape of each system as the mass ratio λ varies. The wave functions or the density distributions for each class of states, identified by the equivalent set of (K,T), (v_2, ℓ_v), or (n_ξ, m) quantum numbers, are displayed together and compared for different λ's at the equivalent hyperradii. In Sec. II A we review briefly the hyperspherical methodology to define the notations used in this work. This is followed by transforming the wave function to the body frame from which the density function at each hyperradius is derived. The results are presented in Sec. III, where we compare the density functions for different channels for various masses of the three-body systems. A short conclusion is given in Sec. IV.

The hyperspherical approach has been applied to the $e^-e^+e^-$ system previously [13] using a different numerical approach. Only $^1P^o$ states were considered.

II. METHODS OF CALCULATIONS

A. Summary of the hyperspherical methodology

For a three-particle system, three sets of Jacobi coordinates can be defined, see Fig. 1. For the present ABA system, the α set corresponds to that used for H_2^+. The β set and γ set coordinates are equivalent under the exchange between the two identical particles; they are the coordinates used for describing the atomic systems such as He and H^-. For each set of Jacobi coordinates we can define two mass-weighted vectors

$$\boldsymbol{\xi}_1 = (\mu_1/\mu)^{1/2}\,\boldsymbol{\rho}_1 \ , \qquad \boldsymbol{\xi}_2 = (\mu_2/\mu)^{1/2}\,\boldsymbol{\rho}_2 \ , \tag{1}$$

where μ_1 and μ_2 are the reduced masses associated with each vector $\boldsymbol{\rho}_1$ and $\boldsymbol{\rho}_2$ (see Fig. 1), respectively, and μ is arbitrary, which was set to unity in this paper. For each set we also define a hyperspherical radius R and a hyperangle ϕ,

$$R^2 = \xi_1^2 + \xi_2^2 \ , \qquad \tan\phi = \xi_2/\xi_1 \ , \tag{2}$$

where the hyperradius R is invariant among the three sets of Jacobi coordinates. In terms of the mass-weighted hyperspherical coordinates the kinetic-energy operator is rewritten as

$$T = -\frac{1}{2\mu}\left(\frac{\partial^2}{\partial R^2} + \frac{5}{R}\,\frac{\partial}{\partial R} - \frac{\Lambda^2(\Omega)}{R^2}\right) \ , \tag{3}$$

where $\Omega = (\phi, \hat{\boldsymbol{\xi}}_1, \hat{\boldsymbol{\xi}}_2)$ are the five angles and Λ^2 is the grand angular momentum operator [see Eq.(4) of Ref. [11]]. The advantage of the mass-weighted hyperspherical coordinates is that except for the trivial mass scaling, the kinetic-energy operator does not depend on the masses of the system. Instead, the masses enter in the potential-energy term.

We solve the Schrödinger equation in hyperspherical coordinates using the adiabatic approximation with the hyperradius as the adiabatic parameter;

$$\Psi(R,\Omega) = \sum_\nu F_\nu(R)\,\Phi_\nu(R;\Omega) \ , \tag{4}$$

where

$$\left(\frac{\Lambda^2(\Omega)}{R^2} + 2\mu\,V(R,\Omega)\right)\Phi_\nu(R;\Omega) = U_\nu(R)\,\Phi_\nu(R;\Omega). \tag{5}$$

In Eq.(5), $V(R,\Omega)=C(\phi,\theta_{12})/R$ is the potential energy of the whole system and C is an effective charge that depends only on the angles ϕ and θ_{12}, where θ_{12} is the angle between the two vectors $\boldsymbol{\rho}_1$ and $\boldsymbol{\rho}_2$. In Ref. [11] the potential curves $U_\nu(R)$ had been calculated for a number of λ's and different total orbital (L) and spin (S_{12}) angular momenta and parity (π). (In designating the total spin angular momentum, we follow the convention used in atoms where the spin of particle B is not included.) Our goal in this paper is to analyze the wave functions $\Phi_\nu(R;\Omega)$ to extract the shape and other properties.

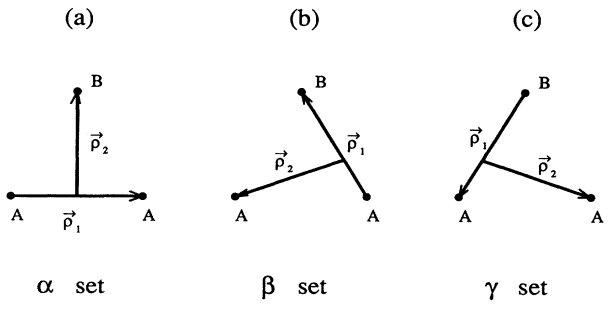

FIG. 1. The three Jacobi coordinates for the three-body systems.

B. Hyperspherical channel functions

The numerical procedure for calculating the channel functions $\Phi_\nu(R;\Omega)$ and the potential curves have been described in Ref. [11]. For the ABA system, the νth channel function is written as the linear combination of basis functions in β- and γ-set coordinates,

$$\Phi_\nu(R;\Omega) = \sum_{\ell_1,\ell_2,n} A_\nu^{\ell_1\ell_2 n}(R)\,[f_L^{\ell_1\ell_2 n}(R;\phi^\beta)\,Y_{\ell_1\ell_2 LM}\,(\hat{\xi}_1^\beta,\hat{\xi}_2^\beta) + (-1)^{\ell_1+S_{12}}\,f_L^{\ell_1\ell_2 n}\,(R,\phi^\gamma)\,Y_{\ell_1\ell_2 LM}\,(\hat{\xi}_1^\gamma,\hat{\xi}_2^\gamma)]\,, \tag{6}$$

where

$$f_L^{\ell_1\ell_2 n}\,(R;\phi) = g_L^{\ell_1\ell_2 n}\,(R;\phi)/\sin\phi\,\cos\phi \tag{7}$$

is the solution of the following equation:

$$\left(-\frac{d^2}{d\phi^2} - \frac{1}{4} + \frac{\ell_1(\ell_1+1)}{\cos^2\phi} + \frac{\ell_2(\ell_2+1)}{\sin^2\phi} + 2\mu R V_c^{\ell_1\ell_2}(R,\phi)\right) g_L^{\ell_1\ell_2 n}(R;\phi) = U_L^{\ell_1\ell_2 n}(R)\,g_L^{\ell_1\ell_2 n}(R;\phi)\,, \tag{8}$$

$$V_c^{\ell_1\ell_2}(R,\phi) = < Y_{\ell_1\ell_2 LM}|RV(R,\Omega)|Y_{\ell_1\ell_2 LM} > \,. \tag{9}$$

The functions $g(R;\phi)$ are calculated by solving Eq. (8) numerically. In the equations above, $Y_{\ell_1\ell_2 LM}$ is the coupled angular momentum function.

To express the channel function in the α-set coordinates, we first expand the basis function f in terms of Jacobi polynomials at a given R,

$$f_L^{\ell_1\ell_2 n}(R;\phi^\beta) = \sum_m b_m^{\ell_1\ell_2 n}(R)\,P_m^{(\ell_2\ell_1)}(\phi^\beta)\,. \tag{10}$$

By using the transformation brackets [14] to rewrite the hyperspherical harmonics in the β- and γ-set coordinates in terms of those in the α-set coordinates, the channel function is then expanded as

$$\Phi_\nu(R;\Omega) = \sum_{\ell_1\ell_2 n} A_\nu^{\ell_1\ell_2 n}(R) \sum_m b_m^{\ell_1\ell_2 n}(R) \sum_{[K'']} a_{[K'']}^{[K]\beta\alpha}\,[1+(-1)^{\ell_1''+S_{12}}]y_{[K'']}(\Omega^\alpha)\,, \tag{11}$$

where a is the transformation bracket that is the overlap between the $y_{[K'']}$ hyperspherical harmonics in the α-set coordinates and the $y_{[K]}$ hyperspherical harmonics in the β-set coordinates

C. Transformation of the wave function to the body frame

In order to study the geometry of a three-body system at each hyperradius R, it is necessary to express the wave function in the body frame. Let $(\hat{\mathbf{i}},\hat{\mathbf{j}},\hat{\mathbf{k}})$ be the three axes of the laboratory frame and $(\hat{\mathbf{i}}'',\hat{\mathbf{j}}'',\hat{\mathbf{k}}'')$ be the same for the body frame. The transformation from the laboratory to the body frame is accomplished by a rotation matrix $R(\alpha\beta\gamma)$ where α, β, and γ are Euler angles. In the body frame, the polar axis $\hat{\mathbf{k}}''$ is defined to be along $\hat{\xi}_1$, and $\hat{\mathbf{i}}''$ is defined such that $\hat{\xi}_2$ is on the $(\hat{\mathbf{i}}'',\hat{\mathbf{k}}'')$ plane. Using this definition, the spherical angles in the body frame are $\hat{\xi}_1 = (0,0)$ and $\hat{\xi}_2 = (\theta_{12},0)$. Thus the Euler angles for the rotation are $\alpha = \phi_1$, $\beta = \theta_1$. The volume element transforms as

$$d\hat{\xi}_1 d\hat{\xi}_2 = \sin\theta_{12} d\theta_{12} \sin\beta\, d\alpha\, d\beta\, d\gamma\,. \tag{12}$$

Using the relation

$$[Y_{\ell_1}(\hat{\xi}_1)Y_{\ell_2}(\hat{\xi}_2)]_{LM} = \sum_Q C_{\ell_1 0\ell_2 Q}^{LQ}\,D_{QM}^L(\omega)\,Y_{\ell_2 Q}(\theta_{12},0)\left(\frac{2\ell_1+1}{4\pi}\right)^{1/2}\,, \tag{13}$$

Eq.(11) is finally written as

$$\Phi_\nu(R;\Omega) = \sum_{\ell_1,\ell_2,n} A_\nu^{\ell_1\ell_2 n} \sum_m b_m^{\ell_1\ell_2 n}(R) \sum_{[K'']} a_{[K'']}^{[K]\beta\alpha}[1+(-1)^{\ell_1''+S_{12}}]P_{m''}^{(\ell_2''\ell_1'')}(\phi^\alpha) \times \sum_Q C_{\ell_1'' 0\ell_2'' Q}^{LQ}\,D_{QM}^L(\omega)\,Y_{\ell_2'' Q}(\theta_{12},0)\left(\frac{2\ell_1+1}{4\pi}\right)^{1/2}\,. \tag{14}$$

D. Density distribution

The surface density distribution is defined as

$$\rho_S(R;\phi^\alpha,\theta_{12}^\alpha) = \int |\Phi_\nu(R;\Omega')|^2\,\delta(\theta_{12}^\alpha - \theta_{12}')\,\delta(\phi^\alpha - \phi')d\Omega' = \sin\theta_{12}^\alpha\,\cos^2\phi^\alpha\sin^2\phi^\alpha \int |\Phi_\nu(R;\Omega)|^2 \sin\beta\, d\alpha\, d\beta\, d\gamma\,. \tag{15}$$

To simplify Eq.(15), we use

$$\int D^{L\,*}_{QM}(\omega)\, D^{L}_{Q'M'}(\omega) \sin\beta\, d\alpha\, d\beta\, d\gamma = \frac{8\pi^2}{2L+1}\,\delta_{Q'Q}\,\delta_{M'M}\ , \tag{16}$$

$$Y_{\ell_2''-Q}(\theta_{12},0)\, Y_{\ell_2'''Q}(\theta_{12},0) = \sum_{L'}\left(\frac{(2\ell_2''+1)(2\ell_2'''+1)}{4\pi(2L'+1)}\right)^{1/2} C^{L'\,0}_{\ell_2''0\ell_2'''0}\, C^{L'0}_{\ell_2''-Q\ell_2'''Q}\, Y_{L'0}(\theta_{12},0)\ , \tag{17}$$

and

$$\sum_{Q}(-1)^{Q}\, C^{L\,Q}_{\ell_1''0\ell_2''Q}\, C^{L\,Q}_{\ell_1'''0\ell_2'''Q}\, C^{L'0}_{\ell_1''-Q\ell_2'''Q} = (-1)^{L+L'}(2L+1)\, C^{L'0}_{\ell_1''0\ell_1'''0}\, W(\ell_1''\ell_2''\ell_1'''\ell_2'''LL')\ , \tag{18}$$

to obtain the final expression

$$\begin{aligned}\rho_S(R;\phi^\alpha,\theta^\alpha_{12}) = &\sum_{\ell_1,\ell_2,n} A^{\ell_1\ell_2 n}_{\nu} \sum_m b^{\ell_1\ell_2 n}_m(R) \sum_{[K'']} a^{[K]\beta\alpha}_{[K'']}[1+(-1)^{\ell_1''+S_{12}}] P^{(\ell_2''\ell_1'')}_{m''}(\phi^\alpha)\\ &\times \sum_{\ell_1',\ell_2',n'} A^{\ell_1'\ell_2' n'}_{\nu} \sum_{m'} b^{\ell_1'\ell_2' n'}_{m'}(R) \sum_{[K''']} a^{[K']\beta\alpha}_{[K''']}[1+(-1)^{\ell_1'''+S_{12}}] P^{(\ell_2'''\ell_1''')}_{m''}(\phi^\alpha)\\ &\times \sum_{L'}(-1)^{L+L'}\sqrt{[(2\ell_1''+1)\,(2\ell_2''+1)\,(2\ell_1'''+1)\,(2\ell_2'''+1)/2]}\, C^{L'0}_{\ell_1''0\ell_1'''0}\\ &\times C^{L'0}_{\ell_2''0\ell_2'''0}\, W(\ell_1''\ell_2''\ell_1'''\ell_2''', LL')\, P_{L'}(\cos\theta^\alpha_{12})\, \sin\theta^\alpha_{12}\cos^2\phi^\alpha \sin^2\phi^\alpha\ .\end{aligned} \tag{19}$$

In the equations above, the C's are the Clebsch-Gordan coefficients and the W's are the Wigner W coefficients.

The above expansion formulas are inaccurate at large R where the expansion equation (10) would require a large number of hyperspherical harmonics. An alternative expansion is used, see the Appendix.

III. SHAPE AND DENSITY FUNCTIONS OF COULOMBIC THREE-BODY SYSTEMS

In this section we examine the density distributions for the channel functions at a fixed hyperradius in the α-set coordinates. Four values of the mass ratio λ were chosen: $\lambda = \frac{1}{3}$, 1, 3, and 17.7. The λ=1 is for the $e^-e^+e^-$ and λ=17.7 is for the $d^+\mu^-d^+$. The other two cases are for fictitious systems, although λ=3 is quite close to a πKK system that has λ=3.53. Typically, 8–12 basis functions in β-set (and γ-set) coordinates are used in each calculation, as in Ref. [11]. The calculated density plots are to be compared at comparable values of the hyperradius for different λ's.

The size of a bound state of an ABA Coulombic three-body system can be estimated from the size of bound states in the two-body system AB. To compare the density plots for different systems in the mass-weighted hyperspherical coordinates, the values of the hyperradius for different λ's have to be suitably scaled. This is best examined in the β-set (or γ-set) coordinates where ρ_1 measures the distance between the pair AB. Recall that in β-set coordinates, $\xi_1 = \sqrt{\mu_1}\ \rho_1$, $\xi_2 = \sqrt{\mu_2}\ \rho_2$, where $\mu_1 = m_A m_B/(m_A+m_B)$ and $\mu_2 = (m_A+m_B)m_A/(2m_A+m_B)$. (All the quantities in this paragraph refer to β-set coordinates.) We consider states where $\rho_1 \cong \rho_2$. In this limit the hyperradius is $R^2 = \mu_1\rho_1^2 + \mu_2\rho_2^2 \cong (\mu_1+\mu_2)\rho_1^2$. The distance ρ_1 between A and B is scaled by its reduced mass, thus $\rho_1 \cong \rho_1(\mathrm{H}^-)/\mu_1$ where $\rho_1(\mathrm{H}^-)$ is the average distance between the electron and the proton in H^-. This simple estimate allows us to express $R \cong (\sqrt{\mu_1+\mu_2}/\mu_1)R(\mathrm{H}^-)$ where $R(\mathrm{H}^-)$ is the hyperradius for the H^- system. The scaling factors $\tau(\lambda) = \sqrt{\mu_1+\mu_2}/\mu_1$ are 1.66, 2.16, 2.09, and 3.35 for $\lambda = \frac{1}{3}$, 1, 3, and 17.7, respectively. We checked and established the validity of this scaling by comparing the values of R where the potential curve reaches the mimimum. (See, for example, the ν=1 and 2 curves shown in Figs. 1 and 7 of Ref. [11].) Thus for the graphs shown below, a value of $R(\mathrm{H}^-)$ is first chosen, the density plot for each λ is then presented for the corresponding value of R where $R = \tau(\lambda)\ R(\mathrm{H}^-)$. The mass of the lighter particle is taken to be unity for each system.

A. Potential surface and density functions of the ground-state channels

As stated earlier, in the mass-weighted hyperspherical coordinates, the kinetic-energy operator is the same for all three-body systems. The differences are in the potential energy, which has the general form $C(\phi,\theta_{12})/R$. As we have shown previously [12], the potential surface exhibits spectacular resemblances in the α-set coordinates. The potential surfaces for the four different λ's are shown in Fig. 2, both in surface plots and in contour plots. The surface plots provide a better perspective, but contour plots give finer details. Since the wave functions at each hyperradius R are eigenfunctions on each potential surface, the nature of the potential surface is used to interpret the calculated density and shape functions of each three-body system.

Each potential surface has a number of features that should be mentioned. The potential is symmetric with respect to $\theta_{12} = 90°$. The interaction between the two identical particles gives rise to a repulsive "wall" at

$\phi = 90°$. The attractive interaction between B and the two identical particles A gives rise to two deep potential valleys at $(\phi°, \theta_{12} = 0°)$ and $(\phi°, \theta_{12} = 180°)$ where $\tan\phi° = \frac{1}{2}\sqrt{(\mu_2/\mu_1)}$. The saddle point of the Coulombic three-body system is at the midpoint of the line connecting the two identical particles. Strictly speaking this saddle point occurs when $\xi_2 = 0$, which is the $\phi = 0$ line in the α-set coordinates. However, a stable oscillation (perpendicular to the line connecting the two identical particles) near the saddle point corresponds to $\theta_{12} = 90°$ and we can take the saddle point to be at $(\phi = 0, \theta_{12} = 90°)$.

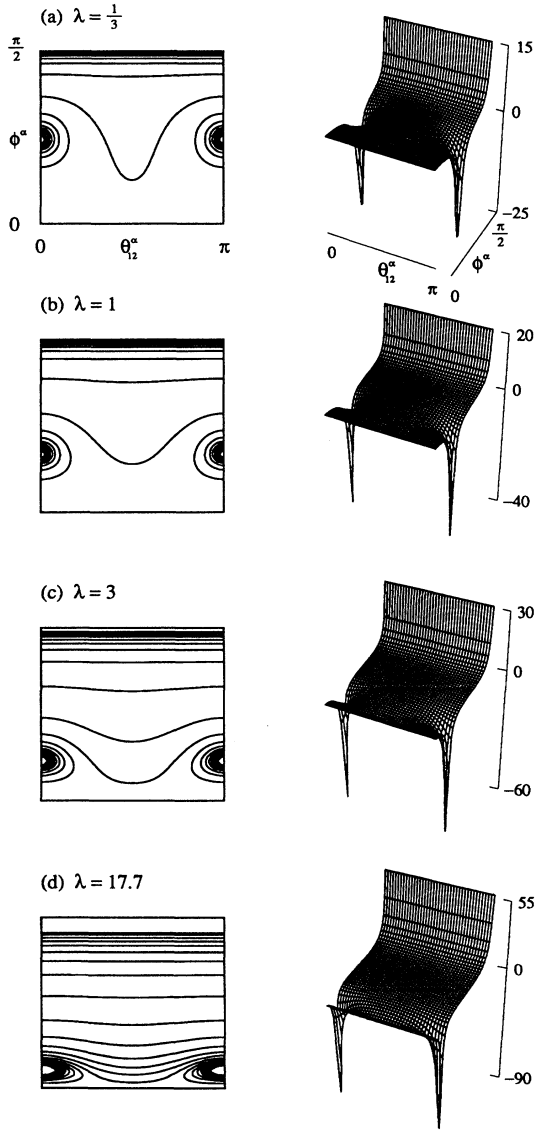

FIG. 2. The potential surface shown on the $(\phi^\alpha, \theta_{12}^\alpha)$ plane of the α-set coordinates at $R = 1$ for $\lambda = \frac{1}{3}$, 1, 3, and 17.7. Both the surface and the contour plots are given. The valleys shift to small values of ϕ^α as λ increases. The saddle point occurs at $\phi^\alpha = 0$ and $\theta_{12}^\alpha = 90°$ for each figure.

The density plots for the adiabatic wave functions belonging to the first potential curve, $\nu = 1$, for $^1S^e$ at $R(\mathrm{H}^-) = 2$ for the four systems are shown in Fig. 3. At this value of $R(\mathrm{H}^-)$, the $\nu = 1$ potential curve for each λ reaches the minimum. These graphs are to be examined with reference to the potential surfaces given in Fig. 2.

To understand these graphs, we first note that the density distribution is determined by the kinetic-energy operator Λ^2/R^2 and by the potential-energy operator C/R [see Eq.(5)]. At large R, where the potential-energy term dominates, the wave function is expected to localize near the valleys of the potential surface. At small R where the kinetic-energy term is dominant, the wave function is represented approximately by the hyperspherical harmonics, which are the eigenfunctions of the kinetic-energy operator Λ^2/R^2. The density plots shown in Fig. 3 are from wave functions at values of R, where contributions from the potential- and kinetic-energy terms are comparable.

The density plots for the four different λ's shown in Fig. 3 have very similar shapes. Since each is derived from the ground-state wave function at the given R, each density function exhibits no nodal lines. Since it is for

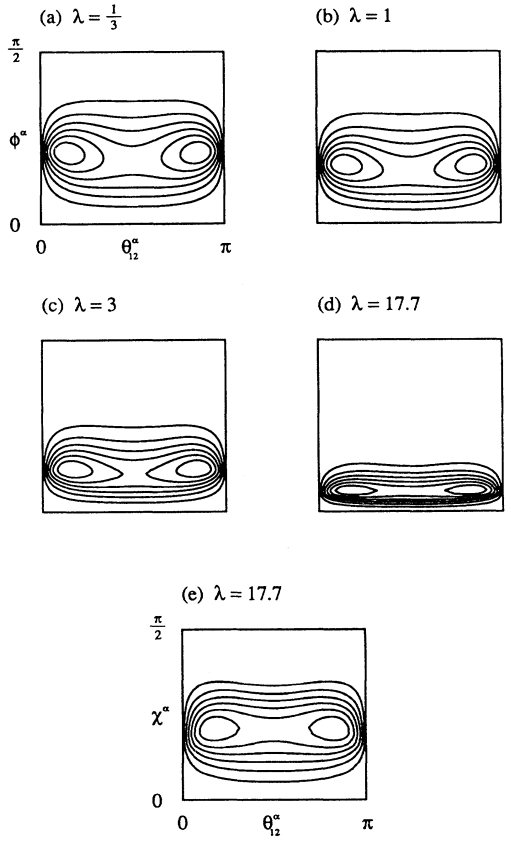

FIG. 3. Density distributions for $^1S^e$ and $\nu = 1$ states for various λ's at $R(\mathrm{H}^-) = 2$. The density does not show any nodal lines for these lowest channels. Note that the density plot for $d\mu d$ can be expressed as in (e) in terms of the two angles (χ, θ_{12}) where angle χ is rescaled from ϕ; see text.

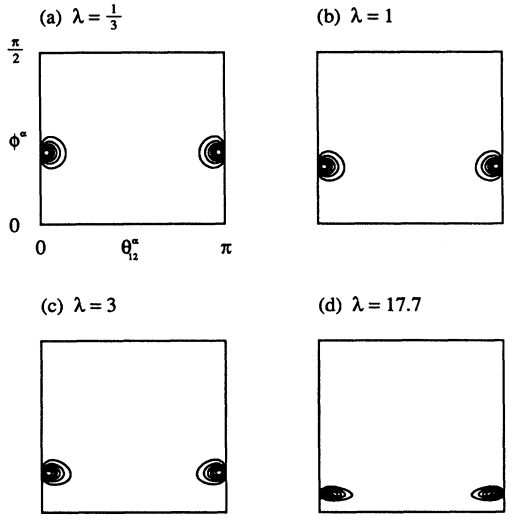

FIG. 4. Same as Fig. 3 but for $R(H^-) = 7.8$. The density distribution is localized at the potential valleys.

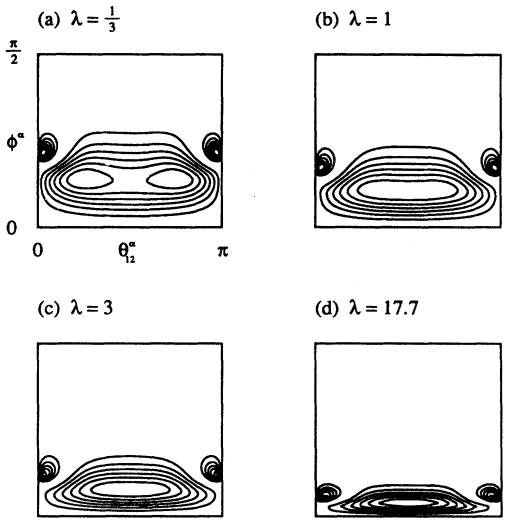

FIG. 5. The density distribution for the $\nu = 2$, $^1S^e$ channel for the various λ's at $R(H^-) = 7.8$. The distributions correspond to particle B, which tends to stay near the midpoint connecting the two identical particles.

$^1S^e$ symmetry, each wave function is symmetric with respect to $\theta_{12} = \pi/2$ and thus $\theta_{12} = \pi/2$ is an anitnodal line. The major difference among the plots is that the density is "squeezed" toward $\phi = 0$ as λ increases. This is the consequence of displaying the density in the mass-weighted hyperspherical coordinates. If one defines a hyperangle χ in terms of actual distances ρ_1 and ρ_2 (in the α-set coordinates) by $\tan\chi = \rho_2/\rho_1 = \sqrt{\mu_1/\mu_2}\tan\phi$, the density in the (χ, θ_{12}) plane would then occupy about the same space. This is illustrated by redrawing the density in the (χ, θ_{12}) plane for the $d\mu d$ system, as shown in Fig. 3(e). The latter occupies about the same space as the one for $\lambda = \frac{1}{3}$ shown in Fig. 3(a).

As the hyperradius increases, the solutions of Eq. (5) become dominated by the potential-energy term such that the wave function is confined to the potential valleys. This is shown by displaying the density functions at $R(H^-) = 7.8$ (Fig. 4). [Recall that the minumum of the potential curve for this channel occurs at $R(H^-) \cong 2$.]

B. Doubly excited channels

We next consider wave functions that belong to resonances associated with the excited states of the AB system. These states correspond to doubly excited states in H^- or to electronically excited states in $H_2{}^+$. In previous studies for H^-, it has been found that these doubly excited states display strong radial and angular correlations. To illustrate the similarity in the shapes for different λ's, in Fig. 5 we show the density plots for the $\nu = 2$ curves for the $^1S^e$ symmetry at $R(H^-) = 7.8$. At this value of $R(H^-)$ the $\nu = 2$ potential curve for each λ reaches the minimum. [The densities for the $\nu = 1$ curve are confined to the potential valleys at this $R(H^-)$ for each λ, as shown in Fig. 4.] It is clear that the density plots for all the λ's are very similar. Again the $\theta_{12} = \pi/2$ line is an antinodal line where the density function peaks at small and moderate values of R. This peak splits into two as R increases. The density distribution consists of the main peak(s) near the saddle point and two minor peaks around the two potential valleys. The density plots also indicate that there is a nodal line separating the peaks around the potential valleys and the main peak(s). The nodal line is expected since this is the first excited channel (ν=2) where the wave function is orthogonal to the ground channel (ν=1). The nodal line is not a straight line, but a curve, indicating the nonseparability of the eigensolutions in the (ϕ, θ_{12}) plane. A more careful inspection reveals that the density tends to maximize near the small $\phi < \phi^\circ$ region. This indicates that the third particle B tends to stay close to the axis connecting the two identical particles A, which corresponds to a bonding configuration in molecules. In the case of H^-, this implies that the two electrons tend to maintain at 180° with respect to the nucleus, and in the case of $H_2{}^+$ the electron tends to remain near the midpoint of the internuclear axis. All the states belonging to the $\nu = 2$ curves shown in Fig. 5 have similar geometrical shapes.

The situation is different for the $\nu = 3$ channel functions, as shown in Fig. 6. We first note that this channel has higher excitation energy than the $\nu = 2$ channel because its density distribution maximizes in the large-ϕ region where the potential is more repulsive. The densities near the saddle point and the small-ϕ region are small. Therefore the $\rho_2 < \rho_1$ region is not occupied and thus particle B is less likely to be found near the line connecting the two identical particles. In this geometry

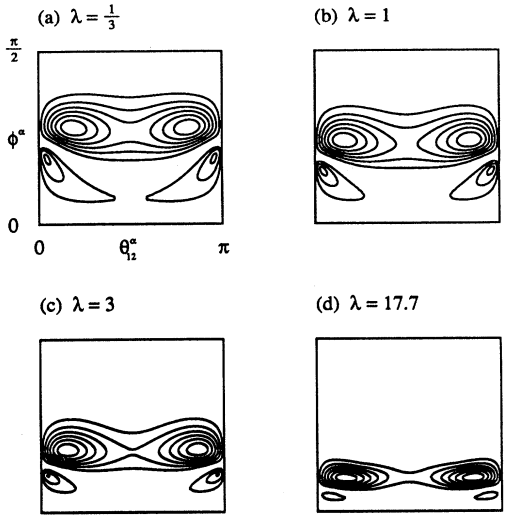

FIG. 6. The density distribution for the $\nu = 3$, $^1S^e$ channel for the various λ's at $R(\mathrm{H}^-) = 7.8$. The distributions correspond to particle B, which tends to stay closer to one of the two identical particles.

the third particle tends to stay closer to one of the two identical particles. Based on the density plots in Fig. 6, one can make quantitative statements. By normalizing the distance between the two identical particles to unity, i.e., $\rho_{AA} = 1$, the most likely geometry of the three-body systems for the cases shown in Fig. 6 is triangles where the base has a unit length, while the two other sides have lengths (1.21, 0.44), (1.26, 0.43), (1.34, 0.48), and (1.50, 0.63), respectively, for $\lambda = \frac{1}{3}$, 1, 3, and 17.7. For such triangles the distance between B and one of the identical particles A is about three times farther than from the other identical particle.

To provide a better perspective of the relative intensities on the (ϕ, θ_{12}) plane, we show the surface plots for the $\nu = 2$ and 3 channels for the $e^-e^+e^-$ system at the values of R given [Fig. 7(a)]. The density distributions are localized at different regions of the plane for the two channels. For $\nu = 2$, the positron tends to stay near the midpoint of the interelectronic axis. In other words, the two electrons tend to stay on opposite sides of the positron. For $\nu = 3$, the positron always stays away from the interelectronic axis. From the viewpoint of the positron, the two electrons tend to stay on the same side of the positron. These two possible types of geometry are identical to those found earlier for H^- (see Fig. 8 of Ref. [2]). We further show in Fig. 7(b) the same two channels for $d\mu d$. The resemblance of the geometry to those shown in Fig. 7(a) is obvious.

C. Density plots along the rotational series

Doubly excited states in H^- and He have been shown to display rotational structures for states that have nearly identical correlations. For the resonances below the $H(\mathrm{n}{=}2)$ thresholds, the $\nu = 2$ curves for $^1S^e$, $^3P^o$, and $^1D^e$ symmetries are known to form a truncated rotor series. This implies that the density plots for these states, after having been averaged over the rotations, are expected to have similar densities. This is illustrated for the $e^-e^+e^-$ [Fig. 8(a)] and $d\mu d$ [Fig. 8(b)] systems. The contour densities and the surface plots are both shown.

From Fig. 8 it is obvious that the major features of the densities for the three different states are identical. The contour plots show that the density tends to spread more and occupies a larger portion of the (ϕ, θ_{12}) plane with increasing L. Thus the increasing rotational angular

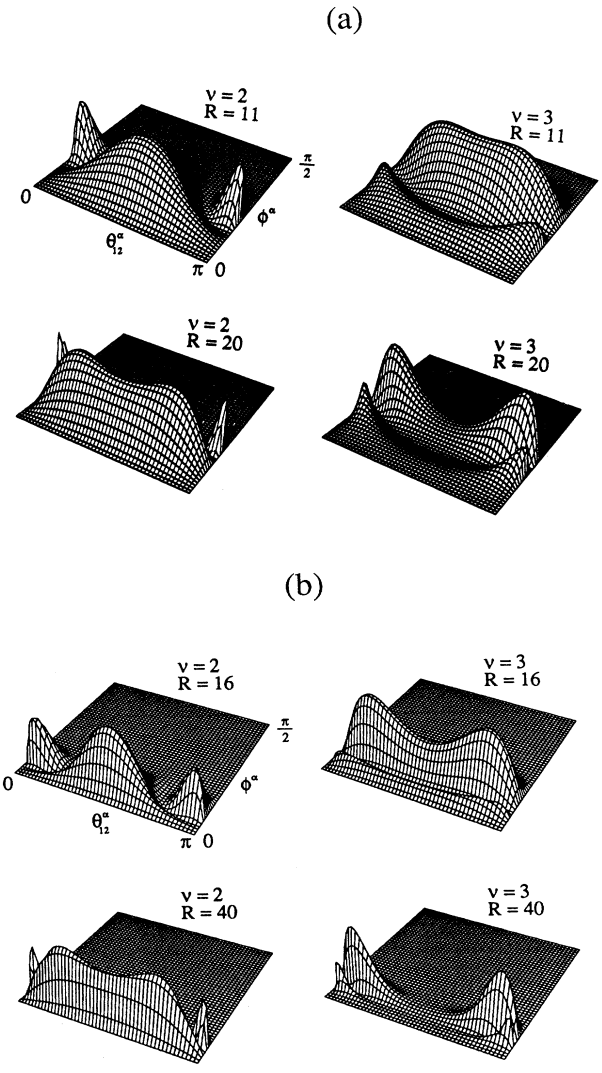

FIG. 7. (a) R dependence of the density distributions for the $\nu = 2$ and 3 channels (of $^1S^e$) for the $e^-e^+e^-$ system. The values of the R's are shown. (b) R dependence of the density distributions for the $\nu = 2$ and 3 channels (of $^1S^e$) for the $d^+\mu^-d^+$ system. The values of the R's are shown.

momentum does not change significantly the shape of the system, in a way similar to that for a semirigid or floppy molecule. This is the origin of the rovibrational energy levels for the Coulombic three-body systems and the results do not depend sensitively on the mass ratio λ.

D. Density plots for $^3S^e$ states

The examples given above dealt mostly with $^1S^e$ states where the wave function is symmetric with respect to the $\theta_{12} = \pi/2$ axis. For $^3S^e$ states, the density plots are very similar to those for the corresponding $^1S^e$ states, except that the wave function is antisymmetric with respect to the $\theta_{12} = \pi/2$ axis. This means that particle B is forbidden on the perpendicular plane which bisects the axis connecting the two identical particles A. Besides this difference, the shape densities are nearly identical. For example, the density plots for the $\nu = 2$ and 3 channels for $^3S^e$ symmetry are shown in Fig. 9. They are very similar to those shown in Figs. 5(b) and 6(b), except for the symmetry with respect to the $\theta_{12} = \pi/2$ axis.

IV. SUMMARY AND CONCLUSIONS

In this paper we examined the geometry of Coulombic three-body systems by displaying the wave functions in mass-weighted hyperspherical coordinates. Within the quasiseparable approximation where each wave function can be expressed as $F_\nu^n(R)\Phi_\nu(R;\Omega)$, information about the shape and the geometry of a Coulombic system is contained in the channel wave function $\Phi_\nu(R;\Omega)$, which has been shown to vary smoothly with R and where the structure of the nodal lines changes adiabatically. We have shown that it is most convenient to display the density distributions in the α-set coordinates (see Fig. 1), especially if one is interested in studying the evolution of the density distributions as the mass ratio λ varies.

We have displayed the density distributions at a fixed hyperradius for a number of channels and examined how

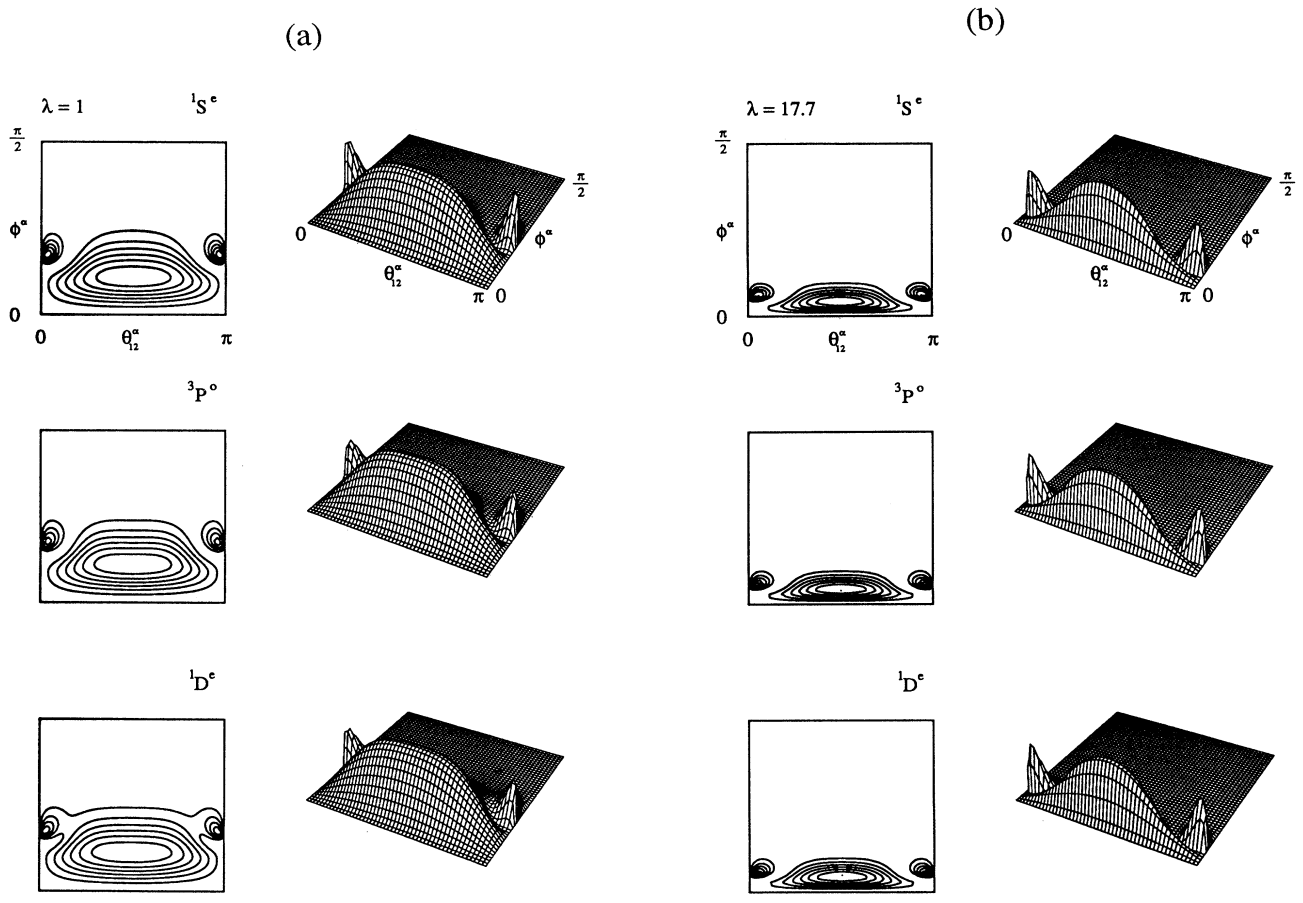

FIG. 8. (a) Density distributions for the $\nu = 2$ channel for $^1S^e$, $^3P^o$ and $^1D^e$ symmetries for the $e^-e^+e^-$ system. Both the surface and contour plots are displayed. (b) The same but for the $d^+\mu^-d^+$ system. Each group belongs to a rotor series and is calculated at $R(H^-)$=7.8.

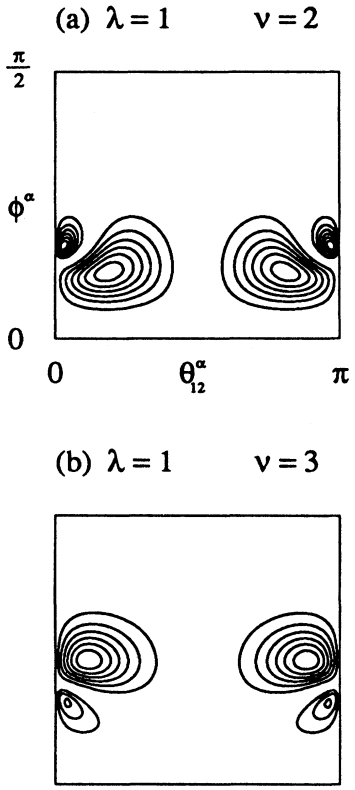

FIG. 9. The density plots for the $\nu = 2$ and 3 channels for the $^3S^e$ symmetry of $e^-e^+e^-$ at $R = 20$. Comparing to Figs. 5(a) and 6(a), the major differences are only in the nodal structure at $\theta_{12} = \pi/2$.

they evolve with the values of λ. For states that belong to the same channel index ν, we showed that the density distribution functions are very similar, implying that the states that are labeled by the same set of quantum numbers have similar geometries. This similarity in the density distribution is further attributed to the similarity in the potential surfaces when the latter are displayed in the α-set coordinates.

From the density distributions, we can further deduce the the geometry of the most likely configurations. We showed that states that have larger density distributions near the saddle point tend to be lower in energy, corresponding to the case where particle B is more likely to be found near the midpoint connecting the line between the two identical particles. The small vibrations of particle B with respect to the saddle point of the potential surface underlies the origin of the rovibrational spectra for the Coulombic three-body systems.

ACKNOWLEDGMENTS

This work is supported in part by the U.S. Department of Energy, Division of Chemical Sciences, and in part by the U.S.-China Cooperative Research Program.

APPENDIX: TRANSFORMATION OF WAVE FUNCTIONS BETWEEN DIFFERENT JACOBI COORDINATES

The expansion given in Eq.(11) suffers from slow convergence at large R. An alternative expansion method is required. To this end, we first rewrite (6) as

$$\Phi_\nu(R;\Omega) = \sum_{\ell_1,\ell_2,n} A_\nu^{\ell_1\ell_2 n} \left(\frac{f_L^{\ell_1\ell_2 n}(R;\phi^\beta)}{\cos^{\ell_1+1}\phi^\beta \sin^{\ell_2+1}\phi^\beta} [\cos^{\ell_1}\phi^\beta \sin^{\ell_2}\phi^\beta \, Y_{\ell_1\ell_2 LM}(\hat{\xi}_1^\beta, \hat{\xi}_2^\beta)] + (-1)^{\ell_1+S_{12}}(\beta \to \gamma) \right) , \quad \text{(A1)}$$

where $(\beta \to \gamma)$ implies that the function in the previous line is repeated except that every quantity in the β-set coordinates is replaced by its equivalent in the γ-set coordinates.

To transform the β-set portion of (A1) to α-set coordinates, we first note that

$$\cos^{\ell_1}\phi^\beta \sin^{\ell_2}\phi^\beta \, Y_{\ell_1\ell_2 LM}(\hat{\xi}_1^\beta, \hat{\xi}_2^\beta) = (\theta_0^{\ell_2\ell_1})^{-1} \sum_{[K'']} a_{[K'']}^{[K]\beta\alpha} y_{[K'']}(\Omega^\alpha) , \quad \text{(A2)}$$

where $\theta_0^{\ell_2\ell_1}$ is the normalization constant of the Jacobi polynomial. This is simply the expansion of the hyperspherical harmonic $y_{[K]}$ for $[K] \equiv [\ell_1, \ell_2, m] = [\ell_1, \ell_2, 0]$ in the β-set coordinates to the hyperspherical harmonics in α-set coordinates.

To transform $f_L^{\ell_1\ell_2 n}(R,\phi)/\cos^{\ell_1+1}\phi \sin^{\ell_2+1}\phi$ from the β-set to α-set coordinates, we utilize the transformation relations between the different Jacobi coordinates. From the geometry, in general,

$$\cos\phi^\beta = (\cos^2\eta_{\alpha\beta}\cos^2\phi^\alpha + \sin^2\eta_{\alpha\beta}\sin^2\phi^\alpha - 2\sin\eta_{\alpha\beta}\cos\eta_{\alpha\beta}\sin\phi^\alpha\cos\phi^\alpha\cos\theta_{12}^\alpha)^{1/2} ,$$

$$\cos\phi^\gamma = (\cos^2\eta_{\alpha\beta}\cos^2\phi^\alpha + \sin^2\eta_{\alpha\beta}\sin^2\phi^\alpha + 2\sin\eta_{\alpha\beta}\cos\eta_{\alpha\beta}\sin\phi^\alpha\cos\phi^\alpha\cos\theta_{12}^\alpha)^{1/2} , \quad \text{(A3)}$$

where

$$\cos\eta_{\alpha\beta} = [m_1 m_3/(m_1+m_2)(m_2+m_3)]^{1/2} ,$$
$$\sin\eta_{\alpha\beta} = [m_2(m_1+m_2+m_3)/(m_1+m_2)(m_2+m_3)]^{1/2} . \quad \text{(A4)}$$

Combining (A2) and (A3), the β-set part of the basic function can be expressed in terms of functions in α-set coordinates. Similar expansion can be carried out for the γ-set part of (A1).

* Permanent address: Institute of High-Energy Physics, Academia Sinica, Beijing, People's Republic of China.

[1] D. R. Herrick, Adv. Chem. Phys. **52**, 1 (1983).
[2] C. D. Lin, Adv. Mol. Phys. **22**, 77 (1986).
[3] R. S. Berry, Contemp. Phys. **30**, 1 (1989).
[4] U. Fano, Rep. Prog. Phys. **46**, 97 (1983).
[5] D.R. Herrick, M.E. Kellman, and R.D. Poliak, Phys. Rev. A **22**, 1517 (1980).
[6] H. J. Yuh, G. S. Ezra, P. Rehmus, and R. S. Berry, Phys. Rev. Lett. **47**, 497 (1981); G. S. Ezra and R. S. Berry, Phys. Rev. A **28**, 1974 (1983).
[7] (a) C.D. Lin, Phys. Rev. A **25**, 76 (1982); (b) **29**, 1019 (1984); (c) Phys. Rev. Lett. **51**, 1348 (1983).
[8] D. R. Herrick and O. Sinanoglu, Phys. Rev. A **11**, 97 (1975).
[9] S. Watanabe and C. D. Lin, Phys. Rev. A **34**, 823 (1986).
[10] (a) J. Feagin and J. S. Briggs, Phys. Rev. Lett. **57**, 984 (1987); (b) Phys. Rev. A **37**, 4599 (1988); (c) J. M. Rost and J. S. Briggs, Z. Phys. D **5**, 339 (1988).
[11] Z. Chen and C. D. Lin, Phys. Rev. A **42**, 18 (1990).
[12] C. D. Lin and X. H. Liu, Phys. Rev. A **37**, 2749 (1987).
[13] J. Botero and C. H. Greene, Phys. Rev. A **32**, 1249 (1985); J. Botero, *ibid.* **35**, 36 (1987).
[14] C.-G. Bao, Y.-P. Gan, and X.-H .Liu, Comput. Phys. Commun. **36**, 410 (1985).